

# Proton-Radiation Tolerant All-Perovskite Multijunction Solar Cells

Felix Lang,\* Giles E. Eperon,\* Kyle Frohna, Elizabeth M. Tennyson, Amran Al-Ashouri, Georgios Kourkafas, Jürgen Bundesmann, Andrea Denker, Kevin G. West, Louise C. Hirst, Heinz-Christoph Neitzert, and Samuel D. Stranks\*

Radiation-resistant but cost-efficient, flexible, and ultralight solar sheets with high specific power ( $\text{W g}^{-1}$ ) are the “holy grail” of the new space revolution, powering private space exploration, low-cost missions, and future habitats on Moon and Mars. Herein, this study investigates an all-perovskite tandem photovoltaic (PV) technology that uses an ultrathin active layer ( $1.56 \mu\text{m}$ ) but offers high power conversion efficiency, and discusses its potential for high-specific-power applications. This study demonstrates that all-perovskite tandems possess a high tolerance to the harsh radiation environment in space. The tests under 68 MeV proton irradiation show negligible degradation (<6%) at a dose of  $10^{13} \text{ p}^+ \text{ cm}^{-2}$  where even commercially available radiation-hardened space PV degrade >22%. Using high spatial resolution photoluminescence (PL) microscopy, it is revealed that defect clusters in GaAs are responsible for the degradation of current space-PV. By contrast, negligible reduction in PL of the individual perovskite subcells even after the highest dose studied is observed. Studying the intensity-dependent PL of bare low-gap and high-gap perovskite absorbers, it is shown that the  $V_{\text{OC}}$ , fill factor, and efficiency potentials remain identically high after irradiation. Radiation damage of all-perovskite tandems thus has a fundamentally different origin to traditional space PV.

## 1. Introduction

Space applications have been a major driver of innovation in photovoltaics (PV) since the first application of silicon solar cells as satellite power supplies in 1958.<sup>[1]</sup> Furthermore, the development of modern multijunction technologies that rely on complementary absorption of sunlight in subcells with staggered bandgaps to minimize thermalization losses has mainly been driven by space applications. Today's state-of-the-art commercially available space PV are III–V/Ge semiconductor-based triple (3J) junction space solar cells that reach efficiencies around 30%.<sup>[2–4]</sup> These high-performance cells require single crystal, low defect epitaxial growth methods, which are inherently expensive. Commercially available III–V on Ge 3J PV comprising InGaP/GaAs/Ge absorbers are grown on Ge substrates. They are

F. Lang, K. Frohna, E. M. Tennyson, L. C. Hirst, S. D. Stranks  
Cavendish Laboratory  
Department of Physics  
University of Cambridge  
JJ Thomson Avenue, Cambridge CB3 0HE, UK  
E-mail: fl396@cam.ac.uk; sds65@cam.ac.uk

G. E. Eperon  
Center for Chemistry and Nanoscience  
National Renewable Energy Laboratory  
15013 Denver West Parkway, Golden CO 80401, USA  
E-mail: giles@swiftsolar.com

G. E. Eperon  
Swift Solar Inc.  
981 Bing St., San Carlos, CA 94070, USA

A. Al-Ashouri  
Young Investigator Group Perovskite Tandem Solar Cells  
Helmholtz-Zentrum Berlin für Materialien und Energie GmbH  
Kekuléstraße 5, 12489 Berlin, Germany

G. Kourkafas, J. Bundesmann, A. Denker  
Helmholtz-Zentrum Berlin für Materialien und Energie GmbH  
Protonen für die Therapie  
Hahn-Meitner Platz 1, 14109 Berlin, Germany

A. Denker  
Beuth Hochschule für Technik Berlin  
Fachbereich II – Mathematik – Physik – Chemie  
Luxemburgerstr. 10, D-13353 Berlin, Germany

K. G. West  
Trisolx LLC  
Los Angeles, CA 90036, USA

L. C. Hirst  
Department of Materials Science and Metallurgy  
University of Cambridge  
27 Charles Babbage Road, Cambridge CB3 0FS, UK

H.-C. Neitzert  
Department of Industrial Engineering (DIIn)  
Salerno University  
Fisciano, SA 84084, Italy

S. D. Stranks  
Department of Chemical Engineering and Biotechnology  
University of Cambridge  
Philippa Fawcett Drive, Cambridge CB3 0AS, UK

 The ORCID identification number(s) for the author(s) of this article can be found under <https://doi.org/10.1002/aenm.202102246>.

© 2021 The Authors. Advanced Energy Materials published by Wiley-VCH GmbH. This is an open access article under the terms of the Creative Commons Attribution License, which permits use, distribution and reproduction in any medium, provided the original work is properly cited.

DOI: 10.1002/aenm.202102246

thus relatively thick ( $>80\ \mu\text{m}$ ) and heavy ( $>30\ \text{mg cm}^{-2}$ ), which limits their specific power to well below  $1\ \text{W g}^{-1}$ . Novel approaches under development use an epitaxial lift-off process to fabricate AlGaP/GaAs/InGaAs (III–V 3J) solar cells<sup>[5,6]</sup> with a specific power of  $\approx 1.7\ \text{W g}^{-1}$ , but their costs are still prohibitive for more ubiquitous use in lower-cost space applications. More cost-efficient single junction thin-film technologies based on a-Si,<sup>[7]</sup> Cu(In,Ga)Se<sub>2</sub><sup>[8]</sup> (CIGS), CdTe,<sup>[9]</sup> perovskite,<sup>[10–17]</sup> and organic<sup>[10,11]</sup> absorbers have been developed and tested for space applications but exhibit lower efficiencies compared to multijunction technologies. Recently, we have therefore tested perovskite/CIGS and perovskite/Si tandem solar cells for their ability to withstand the harsh radiation environment in space. Exposure to harsh radiation leads to the creation and accumulation of recombination centers that diminish device performance, and thus radiation hardness is a fundamental requirement for the adoption of a PV technology in space.<sup>[18]</sup> While we found that the perovskite/CIGS tandem solar cells vastly exceed the radiation hardness of perovskite/Si, we also showed that their resilience to high energetic irradiation is limited by the CIGS subcell, while the perovskite subcell remains largely undamaged.<sup>[18]</sup>

Herein, we assess all-perovskite tandem PV technologies in a two-terminal monolithic architecture for their radiation tolerance using high energy proton irradiation that mimics the radiation environment in space. Unlike perovskite single junction technologies that use only the most compositionally stable perovskite compositions that are known to be radiation hard,<sup>[10–17]</sup> all-perovskite tandem PV technologies rely on tailored low- and high-bandgap perovskite subcells. Because of the high required bromine and tin contents, which could enable halide segregation and oxidation as additional degradation pathways in the two materials, these perovskite compositions have not yet been proposed or tested for space applications.

We, however, demonstrate that the all-perovskite space PV technology possesses a high radiation hardness, not only exceeding proposed perovskite/CIGS tandem PV but also current commercial III–V on Ge-based space PV solutions, which we test and examine under identical conditions as state-of-the-art systems. Using high spatial resolution PL microscopy, we further show that the damage mechanisms in these two material classes, perovskite and III–V semiconductors, are vastly different.

Our measurements thus establish all-perovskite tandem PV technologies as compelling candidates for cost-efficient solutions with prospects to go to the Moon, Mars, and beyond, as well as a key enabling technology for private space exploration that is revolutionizing space economics. All-perovskite-based multijunction technologies are highly efficient but also thin, thus offering high specific power values, a prerequisite to lower launch costs. They can be processed on thin foils unlocking novel form factors and solar sheets that are unrolled or unfolded once launched into space. Flexible solar sheets are an ideal solution to power anything from large space stations and satellites to the next generation of nanosatellites as their energy consumption is steadily increasing with their capabilities along with the burgeoning use of electric propulsion systems.

## 2. Potential of All-Perovskite Tandem Photovoltaics for Space

Monolithic all-perovskite tandem solar cells comprise high- and low-gap perovskite absorbers with bandgaps optimized for maximum efficiency to be between 1.7–1.9 and 1.15–1.29 eV, respectively.<sup>[19,20]</sup> In **Figure 1a**, we sketch a typical layer stack of the cells under investigation comprising ITO/polyTPD/PFN/high-gap-perovskite/LiF/C<sub>60</sub>/PEIE/AZO/ITO/PEDOT:PSS/low-gap-perovskite/C<sub>60</sub>/BCP/Au, that has been shown to allow high power conversion efficiencies  $>23.1\%$  on rigid substrates and  $>21.3\%$  on flexible substrates<sup>[21]</sup> under AM1.5G illumination. Here, the high-gap perovskite ( $E_G^{HG} = 1.73\ \text{eV}$ ) is a dimethylammonium (DMA)-formamidinium-cesium A-site alloyed perovskite containing FA<sub>0.6</sub>CS<sub>0.3</sub>DMA<sub>0.1</sub>PbI<sub>2.4</sub>Br<sub>0.6</sub> (FACsDMApIbBr). A bromine fraction of only 20% out of total halide here minimizes halide segregation under illumination and thus photovoltage losses, while adding DMA increases the bandgap by octahedral tilting to the required 1.7–1.8 eV.<sup>[22,23]</sup> The low-gap perovskite is comprised of FA<sub>0.75</sub>CS<sub>0.25</sub>Sn<sub>0.5</sub>Pb<sub>0.5</sub>I<sub>3</sub> (FACsPbSnI), featuring a bandgap of  $E_G^{LG} = 1.27\ \text{eV}$ . In contrast to perovskite single junction<sup>[13,14,16,17,24]</sup> and perovskite/CIGS<sup>[18]</sup> tandem solar cells that use well-studied compositionally stable radiation-hard perovskite absorber compositions<sup>[10,12,15–17]</sup> with a bandgap of  $\approx 1.6\ \text{eV}$ , the high-gap and low-gap perovskite compositions required for all-perovskite tandem PV thus face additional potential degradation issues under harsh radiation conditions. The phase-separation of mixed perovskites with high bandgap as well as the oxidation of Sn<sup>2+</sup> to Sn<sup>4+</sup> in low-gap perovskites is known to be triggered by intense and/or prolonged illumination,<sup>[22,25]</sup> heat<sup>[26]</sup> or  $\gamma$ irradiation.<sup>[27]</sup> Harsh particle irradiation excites both, the nuclear and electronic subsystems,<sup>[28]</sup> and thus heat as well as charge-induced degradation mechanisms are likely triggered.

The active layer thickness of typical all-perovskite tandem solar cells is  $\approx 1.56\ \mu\text{m}$ , which is much thinner compared to traditional wafer-based c-Si or III–V on Ge PV technologies at thicknesses of around 260 or 80  $\mu\text{m}$ , respectively. One of the thinnest perovskite solar cells reported back in 2015 relied on just 1.4  $\mu\text{m}$  thick PET foils as substrate, reaching a power weight of  $23\ \text{W g}^{-1}$  with an efficiency of 12%.<sup>[36]</sup> Since then, efficiencies of perovskite-based single junction (1J) and especially all-perovskite tandems (2J) have increased to 21.6% and 24.2%,<sup>[32]</sup> rendering these technologies highly interesting for thin, lightweight, large-area space PV modules and solar blankets. To exemplify the potential of emerging perovskite technologies for space applications, we summarize their current efficiency records on the cell level<sup>[32]</sup> and their realistic efficiency potentials<sup>[19,30]</sup> (corresponding to  $\approx 70\%$  of the SQ limiting efficiency, although further material and light management improvements are likely achievable in future) in **Figure 1b**. Both values are projected to AM0 illumination conditions as detailed in the Supporting Information. We compare them to the efficiency and the realistic efficiency potential<sup>[34,35]</sup> (corresponding to  $\approx 95\%$  of the SQ limiting efficiency) of currently commercially available III–V 3J on Ge<sup>[2–4]</sup> and emerging III–V 3J epitaxial-lift off (ELO)<sup>[5,6]</sup> technologies. We note that the current perovskite technology readiness level (TRL) is much lower, with small device areas ( $A \approx 1\ \text{cm}^2$ ) dominating compared to typical 20–30  $\text{cm}^2$  for c-Si or

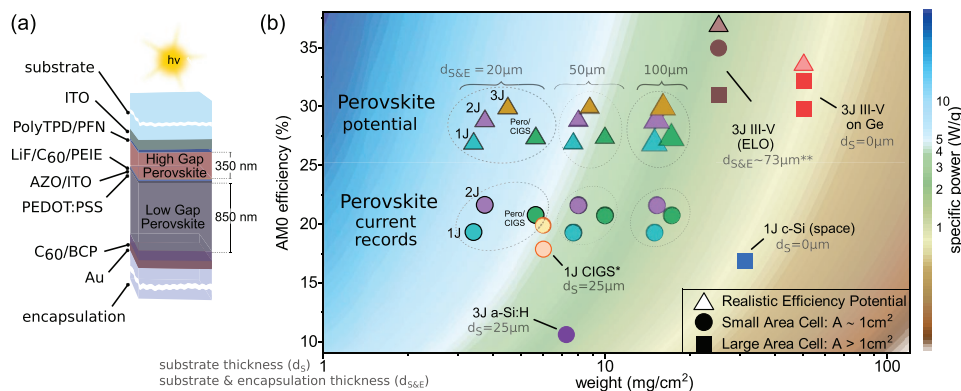


**Figure 1.** Potential of all-perovskite tandem solar cells. a) Sketch of an all-perovskite tandem solar cell (perovskite 2J) comprising FACsDMAPbIBr and FACsPbSnI based perovskite as high-gap and low-gap absorbers, respectively. b) Overview of the efficiency, weight, and specific power potential of perovskite-based 1J, 2J (all perovskite and perovskite/CIGS), and 3J PV based on state-of-the-art small-area lab-scale record efficiencies<sup>[29]</sup> and realistic efficiency potentials<sup>[19,30]</sup> derived from today's materials, corresponding to  $\approx 70\%$  SQ limiting efficiency. As most research reports are based on rigid substrates, we estimate the weight and specific power potential considering the active layer stack and 20–100  $\mu\text{m}$ -thick PI-based substrate and encapsulation foils, as indicated. Values for state-of-the-art commercially available space photovoltaics are based on: III–V 3J on Ge (3G30C, Azur Space,<sup>[2,3]</sup> and Spectrolab XTE-SF<sup>[4]</sup>), III–V 3J (MicroLink,<sup>[5,6]</sup> epitaxial lift-off (ELO)), and c-Si (S32, Azur Space<sup>[2]</sup>) cells. Moreover, we show prominent emerging thin-film technologies, 1J CIGS (\*EMPA<sup>[31]</sup> on flexible polyimide (PI) foil and Solar Frontier<sup>[32]</sup> word record on glass. For both technologies, we assume a weight of 6  $\text{mg cm}^{-2}$  corresponding to the active layer and 25  $\mu\text{m}$  PI foil) and 3J a-Si:H (a-Si:H/a-SiGe:H/a-SiGe:H United Solar Ovonic/UniSolar<sup>[33]</sup>). \*\*In case of the 3J III–V (ELO) cell the packaging weight is  $\approx 10.4 \text{ mg cm}^{-2}$ , corresponding to 73  $\mu\text{m}$  PI foil, but we note that the manufacturer uses a different packaging ( $\approx 40 \mu\text{m}$ ) with identical weight. Finally, we also include a record small area efficiency for III–V 3J, MicroLink, ELO.<sup>[32]</sup> The realistic potential of perovskite 1J, 2J, 3J, and perovskite/CIGS was estimated from refs. [19,30] though we note that further research will be needed to translate small-area performances to modules, and at least a small drop in efficiency is expected. The realistic efficiency potential for lattice-matched III–V on Ge and III–V (no lattice or material constraints) is assumed at 95% of their SQ limiting efficiency following refs. [34,35]. For perovskite- and CIGS-based technologies, and the III–V 3J ELO record<sup>[32]</sup> the AM0 efficiency was projected from reported AM1.5G efficiencies; see the Experimental Section for details. We summarize all values used to produce the figure in Table S1 (Supporting Information).

III–V technologies. Further research on perovskite technologies will be needed to translate small-area performances to larger cell areas and modules, and at least a small drop in efficiency is expected in this translation. Unlike wafer-based III–V on Ge or c-Si technologies that can be handled without support, thin-film PV technologies require a substrate. 10–50  $\mu\text{m}$  thick substrate foils and another 10–50  $\mu\text{m}$  thick encapsulation are realistic estimates and have been successfully used for flexible a-Si:H, GaAs, or CIGS technologies.<sup>[21,37–40]</sup> We believe that known space-tested encapsulation and protection solutions can be transferred to perovskite-based solar cells but note that this needs to be tested thoroughly. While we detail key requirements and potential substrate and encapsulation solutions for space in section 5, we plot in Figure 1b the weight and specific power for the perovskite technologies on the cell level assuming total substrate and encapsulation thicknesses of  $d_{S,E} = 20, 50,$  or 100  $\mu\text{m}$ , as indicated. The mass of any thin-film PV module is dominated by its packaging, i.e., substrate, encapsulation, while interconnects and busbars add negligible extra weight when using monolithic interconnections.<sup>[35]</sup> Under this assumption, we identify all-perovskite tandems as having the highest specific power potential for next-generation space-PV solutions. Their specific power potential is significantly above other thin-film PV technologies currently in consideration for ultralight space photovoltaics, such as 3J a-Si:H, 1J CIGS,<sup>[8]</sup> or 3J III–V technologies with epitaxial lift-off.<sup>[5,6]</sup>

All-perovskite-based 1J and 2J PV technologies are close to commercialization,<sup>[30]</sup> and production costs are expected to be well below existing silicon technologies.<sup>[41]</sup> Perovskite-based space PV thus represent an extremely promising flexible,

ultralight, and cost-efficient technology. Solar sheets that are unrolled or unfolded once launched into space will revolutionize the space PV sector, provided that their tolerance to the harsh radiation environment in space can be proven.

### 3. Proton Radiation Hardness of Perovskite 2J Tandem Photovoltaics

To assess the radiation hardness of all-perovskite 2J tandem solar cells, we fabricate tandem devices with solution-processed high-gap and low-gap perovskite absorbers with the bandgaps and compositions detailed above (see the Supporting Information for experimental details) and bombard the cells with high energy proton irradiation. The radiation environment in space comprises a polyenergetic spectrum of  $e^-$ ,  $H^+$ ,  $He^+$ , and heavier elements. High-energy electrons are far less damaging than high-energy protons, while the flux of heavier particles is orders of magnitude lower. Proton irradiation, therefore, closely mimics the real radiation environment in space. To avoid convoluting effects from oxygen or moisture and radiation-induced color centers in the glass substrate,<sup>[13]</sup> we prepared and encapsulated our tandem solar cells using quartz glass and note that commonly used low energetic protons ( $<10 \text{ MeV}$ ) would be stopped by such substrate and encapsulation solutions and thus are not used in our tests to probe the device layers. Therefore, we use high energy (68 MeV) proton irradiation that can penetrate millimeter-thick substrate and encapsulation layers to test the radiation hardness of our all-perovskite 2J tandem solar cells and compare the results to commercially available

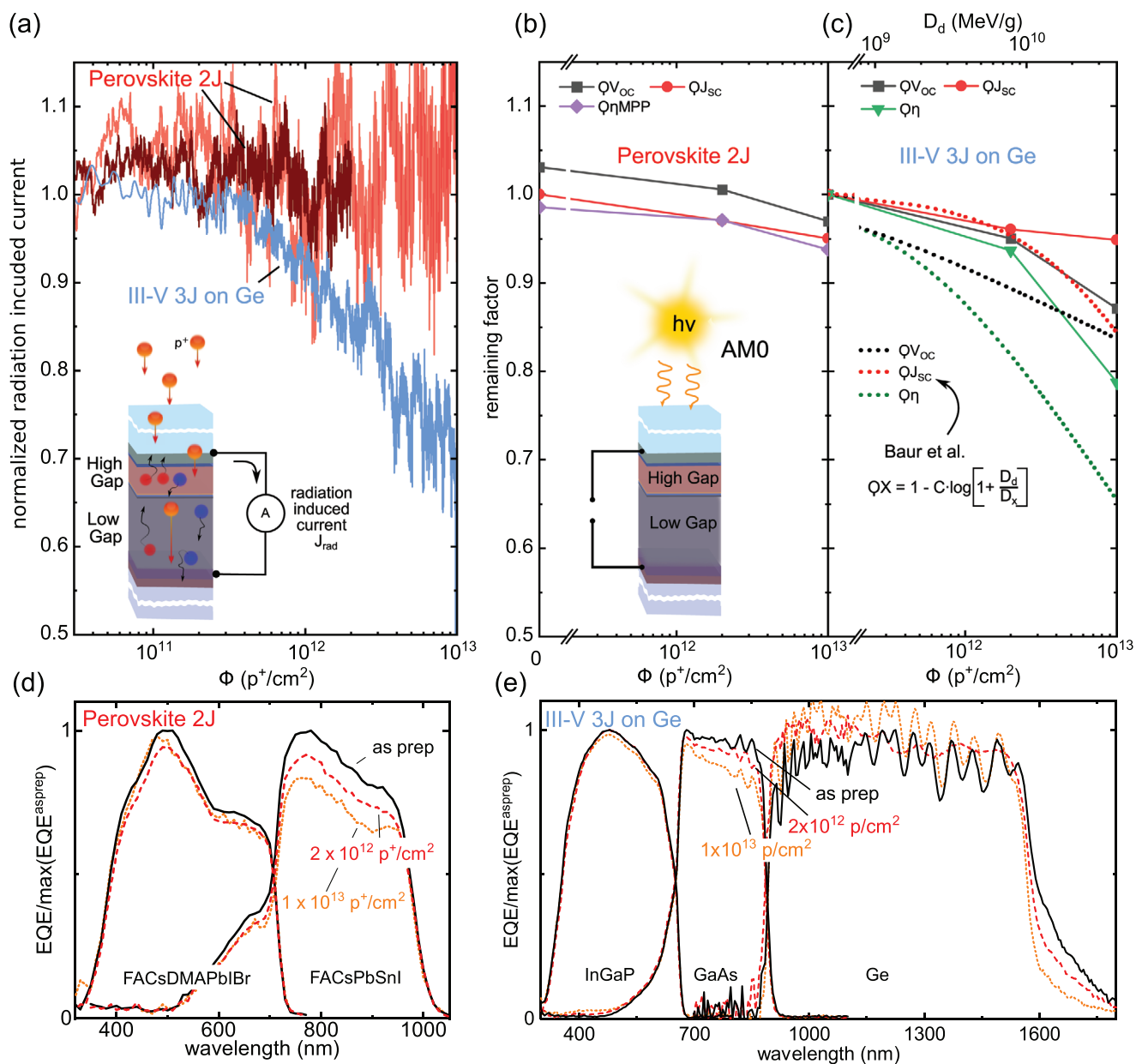


**Figure 2.** Radiation hardness of perovskite 2J solar cells under 68 MeV proton irradiation in comparison with III–V 3J on Ge. a) Degradation of the proton-induced current measured in situ during 68 MeV proton irradiation for two perovskite 2J solar cells (brown and red lines) and a commercial III–V 3J on Ge solar cell, 3G28C Azur Space (blue line). b,c) Remaining factor ( $Q$ ) of  $V_{OC}$ ,  $J_{SC}$ , and  $\eta$  of perovskite 2J and III–V 3J on Ge solar cells as a function of 68 MeV proton fluence under AMO illumination conditions as solid red, black, and purple lines, respectively. Due to potential transient effects in the perovskite 2J tandem, we derived the efficiency by maximum power point (MPP) tracking. For the III–V 3J on Ge case, we further relate the 68 MeV proton fluence to the non-ionizing displacement damage dose ( $D_d$ ) following Akkerman et al.,<sup>[42]</sup> top X-axis and plot literature data on the  $V_{OC}$ ,  $J_{SC}$ , and  $\eta$  remaining factors of III–V 3J on Ge solar cells (3G28C, Azur Space) as a function of  $D_d$ , according to Baur et al.<sup>[43]</sup> (Supporting Information). d,e) Change in external quantum efficiency (EQE) as  $EQE/\max(EQE^{\text{asprep}})$  of the perovskite 2J tandem and III–V 3J on Ge solar cell. Non-normalized data are depicted in Figures S2 and S3 (Supporting Information). Note that the Ge subcell EQE has been corrected from typical measurement artifacts that arise from low shunt resistances and low breakdown voltages prior to normalization following literature procedures,<sup>[44,45]</sup> as detailed in the Supporting Information.

state-of-the-art and well-studied III–V 3J solar cells (3G28C, Azur Space).

We perform tests in operando by monitoring the radiation-induced current during proton irradiation, which we have shown previously to be highly sensitive to the formation of

radiation-induced defects from displacement and ionization damage.<sup>[14]</sup> As shown in **Figure 2a**, blue line, we observe a significant degradation in III–V on Ge based 3J solar cells to about 70% of their initial value after an accumulated proton dose of  $1 \times 10^{13} \text{ p}^+ \text{ cm}^{-2}$ , that, as we detail further below, corresponds

to an accumulated proton dose after about 100 years in low-earth-orbit or ten years in a geostationary orbit. This decrease in performance is indicative of the formation of a considerable number of radiation-induced defects in the device stack. Due to the monolithic interconnection of the subcells, these observations alone do not allow us to identify which subcell is limiting the performance; indeed, radiation-induced degradation in just one subcell could dominate the overall degradation. For perovskite 2J tandem solar cells (red and brown line in Figure 2a), we do not observe any degradation of the normalized radiation-induced current, indicating a superior tolerance to the harsh radiation environment in space. We note that the perovskite 2J tandem solar cells studied here have an order of magnitude smaller active area than the studied III–V 3J on Ge devices, giving rise to the difference in noise between the two systems after normalizing; we plot non-normalized less-noisy data in Figure S1 (Supporting Information).

We corroborate the superior radiation hardness of the perovskite 2J solar cells by current–voltage ( $JV$ ) characteristics measured before and after proton irradiation at an accumulated dose of both  $2 \times 10^{12}$  and  $1 \times 10^{13} \text{ p}^+ \text{ cm}^{-2}$ . Inelastic nuclear scattering of 68 MeV proton irradiation can create short-living isotopes, and, therefore, the ex situ measurements after tests could only be performed once the remaining activity dropped to a safe level, after  $\approx 10$  days. Figure 2b depicts the evolution of the open-circuit voltage ( $V_{OC}$ ), the short-circuit current ( $J_{SC}$ ), and the efficiency derived from a maximum power point tracking ( $\eta_{MPP}$ ) of the perovskite 2J tandem solar cells. To accentuate the small changes, we calculated the remaining factor  $QX$  for all individual metrics  $X$  by  $QX = X_{\text{irradiated}}/X_{\text{as-prepared}}$  and note that the data point at  $\Phi = 0$  refers to a reference device that has not been irradiated but measured before and after the experiment alongside the irradiated samples. We find that even after an accumulated dose of  $1 \times 10^{13} \text{ p}^+ \text{ cm}^{-2}$ , the perovskite 2J tandem PV efficiency has minimally degraded and retains 94% of its initial value. The tested III–V 3J solar cells on Ge, in contrast, degraded to less than 78% (solid lines in Figure 2c). Calculating the displacement damage  $D_d$  (see the Experimental Section) allows us to plot literature data on the degradation of the  $V_{OC}$ ,  $J_{SC}$ , and  $\eta$  of III–V 3J on Ge technologies, according to Baur et al.<sup>[43]</sup> as dashed lines in Figure 2c, suggesting a slightly higher degradation down to 65% of the initial value. To put this degradation into context, a displacement damage  $D_d$  of  $\approx 10^{10} \text{ MeV g}^{-1}$  corresponding to  $\approx 2 \times 10^{12} \text{ p}^+ \text{ cm}^{-2}$  at  $E_p = 68 \text{ MeV}$  is reached during  $\approx 100$  years in a low earth orbit,  $\approx 10$  years in a geostationary orbit, or  $\approx 1$  year in a harsher radiation environment, e.g., found on a mission to Jupiter's moon Europa.<sup>[46]</sup> Note that, depending on the orbit/trajectory, atomic oxygen, deep UV, and extreme temperatures, among others, pose additional challenges that we discuss at the end of this paper. Nevertheless, these results demonstrate the superior radiation hardness to high energetic proton irradiation that mimics the harsh radiation environment in space of perovskite 2J devices over the current industry-standard technology. All-perovskite tandem PV thus also exceeds the radiation hardness of emerging perovskite/Si and perovskite/CIGS tandem PV that degrade by  $\approx 99\%$  and  $\approx 15\%$ , respectively, at  $2 \times 10^{12} \text{ p}^+ \text{ cm}^{-2}$ , a five times lower proton dose than employed in this work.<sup>[18]</sup>

In both the perovskite 2J tandem and the III–V 3J on Ge solar cell cases, we notice a discrepancy between the degradation of the radiation-induced current measured in situ, and the short-circuit current measured ex situ after irradiation under AM0 illumination. This discrepancy is indicative of an unbalanced degradation of the subcells under proton irradiation. Figure 2d,e depicts the external quantum efficiency (EQE) measured prior to and after proton irradiation of both systems. To identify radiation-induced damage, we normalized the subcell EQEs to their maximum EQE value measured prior to irradiation. In the case of the perovskite 2J solar cell, the data clearly reveal that the high-gap top cell is unaffected. The integrated EQE of the low-gap Pb–Sn alloyed bottom cell, in contrast, reduces slightly to about 90% and 83% of the initial values after  $2 \times 10^{12}$  and  $1 \times 10^{13} \text{ p}^+ \text{ cm}^{-2}$ , respectively. In the case of the III–V 3J on Ge, we identify significant degradation specifically within the GaAs middle cell, which is in line with literature reports of III–V on Ge space PV under high energy irradiation.<sup>[47,48]</sup> The spectral response of the InGaP and Ge subcell are barely affected, but in the latter case, we notice a reduction of the indirect gap ( $E_{\text{indirect, gap}}(\text{Ge}) = 0.62 \text{ eV}$ )<sup>[49]</sup> absorption features with increasing proton dose, while above the direct gap of Ge ( $E_{\text{direct, gap}}(\text{Ge}) = 0.81 \text{ eV}$ )<sup>[49]</sup> the spectral response increases again to its initial value. Due to the low intensity of the solar spectrum in that region, this has little to no effect on the integrated current but nevertheless points towards some radiation-induced changes in the Ge subcell that, to our knowledge, has not been described yet.

To exclude that uneven radiation damage is the cause for the higher degradation of the perovskite bottom subcell compared to the perovskite top subcell, we simulated the damage profile generated under 68 MeV proton irradiation using the stopping and range of ions in matter (SRIM) package.<sup>[50]</sup> As detailed in the Supporting Information, this allows us to estimate the non-elastic damage due to nuclear scattering that is known to dominate solar cell degradation.<sup>[51]</sup> We plot the energy loss within the individual layers in Figure 3a and find a relatively homogeneous damage profile over the entire layer, so the damage profile cannot explain the higher damage observed in the low-gap subcell. We further simulated the expected damage from a true space environment considering polyenergetic proton irradiation with differential fluences for an ISS, Starlink, and Europa orbit (Figure 3b). Considering omnidirectional irradiation over a  $4\pi$  solid angle through a 50- $\mu\text{m}$ -thick cover foil, a realistic estimate that has successfully been used for flexible a-Si:H or CIGS technologies,<sup>[21,37–40]</sup> we find an equally homogeneous damage throughout the perovskite tandem solar cell. For a wide range of likely space environments, the expected radiation damage is therefore well mimicked by the homogeneous damage from the monodirectional 68 MeV proton irradiation conditions used here. Considering only “front side” irradiation distributed over a  $2\pi$  solid angle, e.g., in the radiation environment on the Mars surface, we find a twofold higher energy loss of the incident protons within the top cell compared to the bottom cell. According to the EQE measurements shown in Figure 2d, the high-gap perovskite subcell is more radiation hard than the low-gap subcell, and thus we consider this increased dose in the high-gap subcell will not lead to appreciable additional damage.

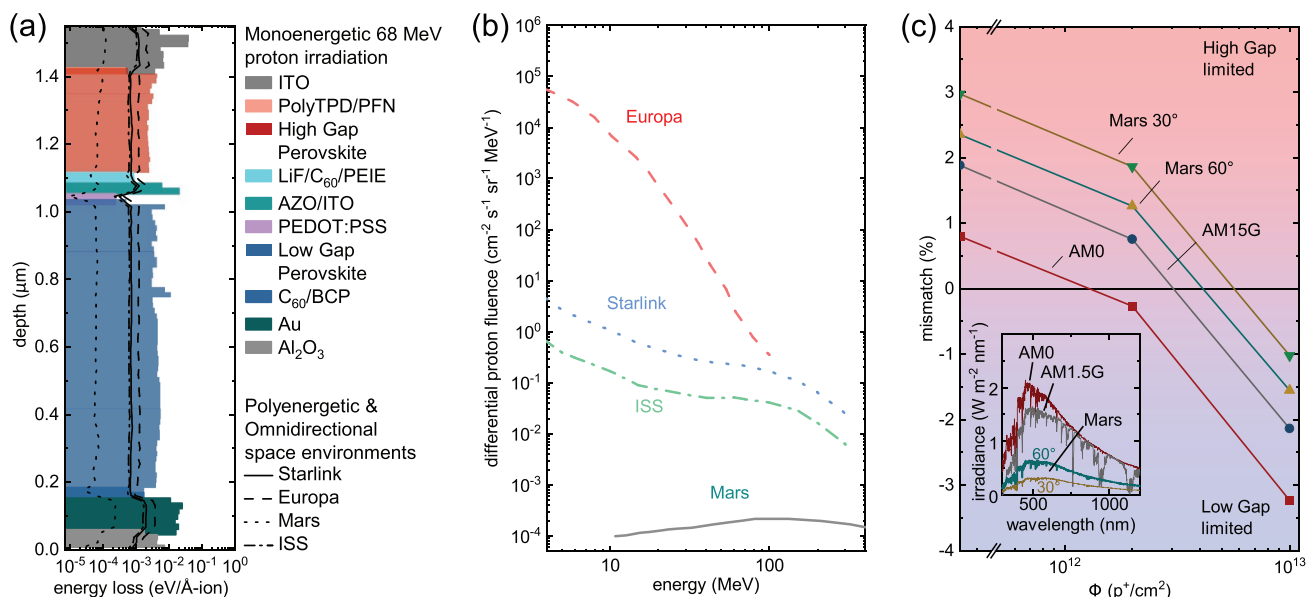


**Figure 3.** Radiation-induced degradation of perovskite 2J tandem solar cells in various space environments. a) SRIM simulation of the non-ionizing energy loss within perovskite 2J tandem solar cells as a function of depth under monoenergetic 68 MeV proton irradiation. Dashed and solid lines depict the approximated energy loss from polyenergetic and omnidirectional proton irradiation, as found in a Starlink, Europa, and ISS orbit. See the Experimental Section for calculation and approximation details. b) Differential proton fluence of the International Space Station (ISS),<sup>[52]</sup> Starlink,<sup>[52]</sup> and Europa<sup>[53]</sup> orbits and the surface of Mars,<sup>[54]</sup> according to data from indicated references. c) Current mismatch of the investigated perovskite 2J tandem solar cells under AM0, AM1.5G, Mars 30°,<sup>[55]</sup> and Mars 60°<sup>[55]</sup> illumination conditions. Positive values represent a limitation by the high-gap top junction, whereas negative values correspond to a limitation by the low-gap bottom junction.

To estimate how the unbalanced subcell degradation affects the overall performance of a monolithic perovskite 2J tandem solar cell, we calculated the spectral mismatch as a function of accumulated proton dose  $\Phi$  (Figure 3c). Under AM0 illumination conditions prior to irradiation we find the evaluated perovskite tandem to be slightly limited by the high gap subcell and, thus, the impact of the degrading low-gap subcell on tandem performance is somewhat dampened, but we still notice a detrimental impact on  $J_{SC}$  and  $\eta$  as described earlier. This dampening effect is enhanced under AM1.5 or Mars 30° and Mars 60° illumination conditions, where the perovskite 2J tandem is strongly limited by the high-gap subcell prior to irradiation with up to 3% mismatch. Indeed, we find negligible degradation of the monolithic perovskite 2J tandem when analyzing the remaining factor of  $\eta_{MPP}$  and  $J_{SC}$  under AM1.5 illumination (Figures S4 and S5, Supporting Information).

### 3.1. Identifying Radiation-Induced $V_{OC}$ Losses in Perovskite 2J Tandem PV

To determine the origin of the small degree of radiation-induced damage in the monolithic perovskite 2J tandem solar cell, we measure the  $V_{OC}$  potential in each subcell by probing their absolute photoluminescence (PL) spectrum. The spontaneous emission of photons from a direct semiconductor is, according to Würfel's generalized Planck law,<sup>[56]</sup> a function of the chemical potential of the non-equilibrium charge carrier concentration, i.e., the quasi-Fermi level splitting (QFLS). Probing the absolute PL spectrum is thus an elegant non-contact method to measure the QFLS and the  $V_{OC}$  potential.<sup>[57–59]</sup>

We do this under 1-sun equivalent illumination conditions, and by fitting the high-energy slope of the PL spectrum, see the Supporting Information for experimental and calculation details. To distinguish between the individual subcell losses, we excite the individual absorber layers selectively by excitation from the front and backside using a  $\lambda = 405$  nm laser, as illustrated in Figure 4a. Our measurements identify a decrease of the low-gap PL intensity after proton irradiation (red lines in Figure 4a). This PL reduction corresponds to a small QFLS loss of 40 meV after a proton dose of  $1 \times 10^{13} \text{ p}^+ \text{ cm}^{-2}$ , suggesting the presence of some radiation-induced damage that leads to increased nonradiative recombination in line with the reduced EQE of the low-gap subcell. Surprisingly, we observe an increase of the high-gap PL intensity, blue lines in Figure 4a, following proton irradiation corresponding to an increase in QFLS by around 20 meV after a dose of  $1 \times 10^{13} \text{ p}^+ \text{ cm}^{-2}$ .

The recombination in halide perovskite solar cells, however, can be dominated by recombination at the interfaces with the respective contact layers.<sup>[57]</sup> To disentangle the underlying mechanisms, we prepared and irradiated bare high-gap and low-gap films (with no contact layers) of otherwise identical compositions on quartz substrates (Figure 4b). Interestingly, the absolute PL of the bare low-gap perovskite remains unchanged, and thus we calculate an identically high QFLS of the low-gap perovskite. The reductions observed within the tandem layer stack, therefore, must originate from radiation-induced damage of the contact layers or their interfaces, while the low-gap perovskite absorber itself remains free of radiation-induced defects even at the highest accumulated dose tested. Note that regardless of any potential radiation damage,

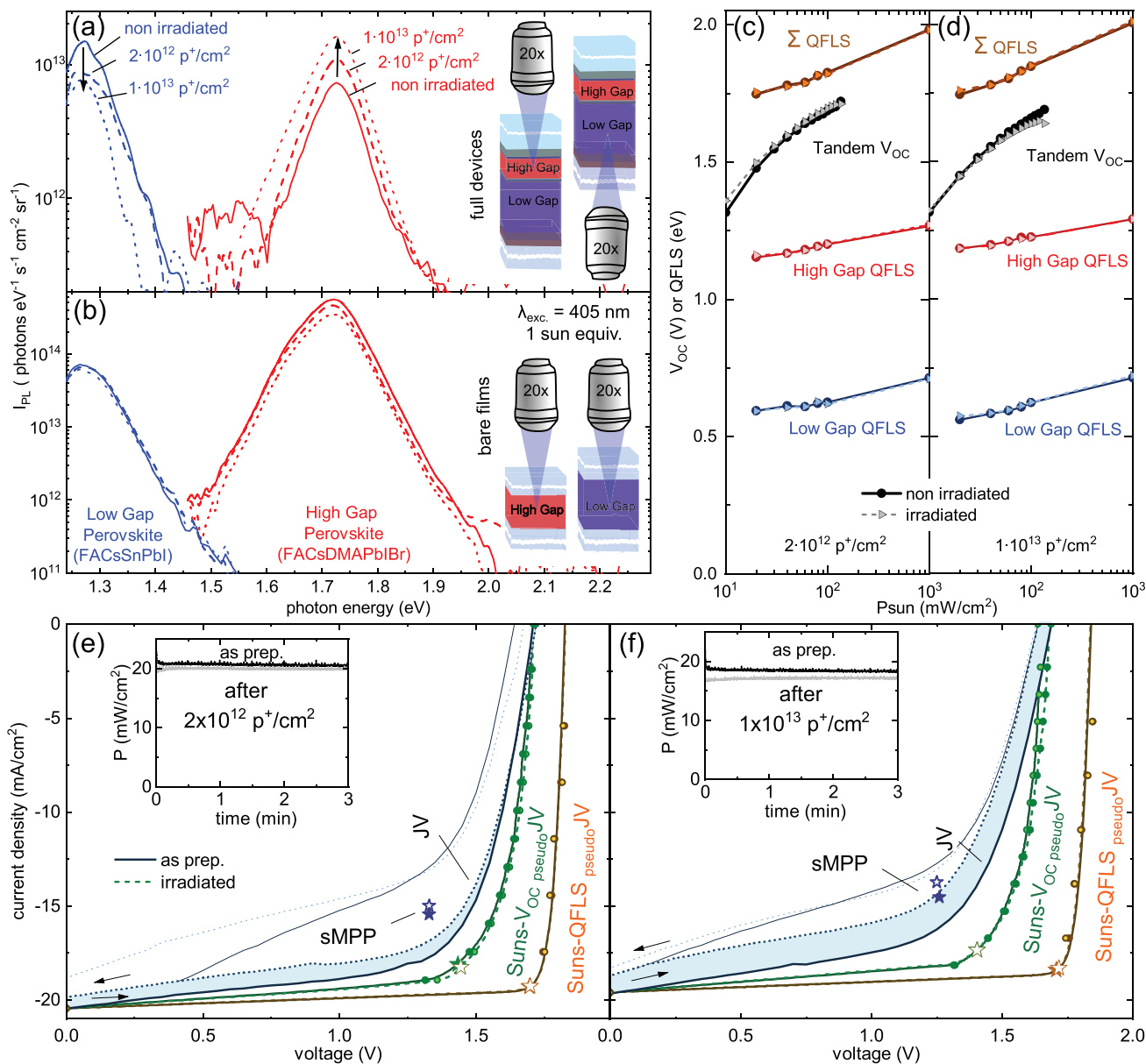


**Figure 4.** Identifying and quantifying radiation-induced losses in perovskite 2J solar cells. a) Absolute PL spectra of the high-gap (FACsDMAPbIBr) and low-gap (FACsPbSnI) absorbers within the perovskite 2J solar cells after proton irradiation. Measurements were performed by excitation with a 405 nm laser set to an equivalent fluence of 1 sun ( $\text{AM1.5G}$ ,  $100 \text{ mW cm}^{-2}$ ) from the top or bottom side, as indicated. b) Absolute PL spectra of bare high-gap (FACsDMAPbIBr) and low-gap (FACsPbSnI) absorbers on quartz. c,d) Suns- $V_{\text{OC}}$  measurements of perovskite 2J tandem solar cells prior to and after proton irradiation with c)  $2 \times 10^{12}$  and d)  $1 \times 10^{13} \text{ p}^+ \text{cm}^{-2}$  as solid black and dashed gray lines, respectively. Suns-QFLS data of the bare low-gap and high-gap absorbers on quartz are shown in blue and red, respectively. To illustrate the  $V_{\text{OC}}$  potential, we further plot the sum of the respective low- and high-gap QFLS in brown. e,f) Measured current-voltage characteristics under AM0 illumination conditions prior to and after proton irradiation compared to pseudo-JV curves calculated from Suns- $V_{\text{OC}}$  and Suns-QFLS data shown in (b). The accumulated proton dose was e)  $2 \times 10^{12}$  and f)  $1 \times 10^{13} \text{ p}^+ \text{cm}^{-2}$ . Insets depict results from maximum power point tracking, and stars denote the stabilized MPP values.

the contact layers quench emission in the active layers, as can be seen in the one order of magnitude higher PL intensities of the bare films compared to measurements on full devices. Finally, we do not observe an increase in PL after irradiation for the high-gap absorber when irradiated and probed as a bare film, suggesting that the increase in PL in the high-gap material after irradiation in the device stack could also be attributed to a change of the contact layers.

### 3.2. Efficiency and Radiation-Hardness Potential of Perovskite 2J PV

To better understand the impact of radiation-induced defects, we need to disentangle nonradiative bulk and interface recombination mechanisms that define the fill factor (FF), ideality factor ( $n$ ), and efficiency ( $\eta$ ). We do this by comparing the intensity dependence of the stabilized  $V_{\text{OC}}$  (Suns- $V_{\text{OC}}$ ) of

complete devices to the intensity dependence of the PL and thus QFLS (Suns–QFLS) of bare high- and low-gap films in Figure 4c.<sup>[60]</sup> We start our analysis by considering the change in the Suns– $V_{OC}$  dependence of as-prepared and irradiated perovskite 2J tandem solar cells for irradiation doses of  $2 \times 10^{12} \text{ p}^+ \text{ cm}^{-2}$  (E) and  $1 \times 10^{13} \text{ p}^+ \text{ cm}^{-2}$  (F). In monolithically interconnected tandem solar cells, the overall ideality factor  $n$  is given by the sum of the individual subcell ideality factors ( $n_i$ ), and thus we expect:  $2 < \sum n_i < 4$  considering  $n = 1$  for ideal band-to-band recombination and  $n = 2$  in the presence of deep recombination centres in each sub-cell.<sup>[18,61]</sup> Interestingly, in as-prepared devices, we observe high ideality factors  $>8$  for both cases, indicating a high shunt contribution. Curiously, the ideality factor decreases upon irradiation. We observed similar improvements in perovskite single junction solar cells after proton irradiation and previously suggested a partial compensation of as-prepared deep traps by radiation-induced shallow defects,<sup>[62]</sup> but also healing mechanisms triggered after proton irradiation might play a role,<sup>[13]</sup> which we discuss later. More information on the dominating recombination mechanisms in the bulk of the individual absorber layers can be gained from the Suns–QFLS dependence of bare high- and low-gap films. We plot these data as red and blue lines with closed dots (as prepared) and open triangles (irradiated) in Figure 4c (see Figure S6, Supporting Information, for an example of the raw intensity-dependent absolute PL spectra). In both the high- and the low-gap case, we observe no significant change in the individual Suns–QFLS dependence upon proton irradiation, suggesting that there are negligible radiation-induced defects that cause additional nonradiative recombination in the perovskite bulk; this is consistent with the negligible change in PL of the neat films (cf. Figure 4b). As summarized in Table S1 (Supporting Information), we observe no significant change in the ideality factors derived from the shown Suns–QFLS dependence. To go one step further, we sum the QFLS of the two individual absorber layers (Figure 4c,d). This allows us to predict the maximum possible  $V_{OC}$  potential of a perovskite 2J tandem solar cell as a function of illumination intensity. Following Stolterfoht et al.,<sup>[60]</sup> we extract pseudo- $JV$  curves from the summed Suns–QFLS and compare them to pseudo- $JV$  curves extracted from the Suns– $V_{OC}$  dependence. In contrast to  $JV$  measurements under illumination, pseudo- $JV$  curves derived from Suns– $V_{OC}$  are unaffected by transport losses. Pseudo- $JV$  curves from Suns–QFLS measurements of bare perovskite absorbers are additionally unaffected by the various contact layers.<sup>[60]</sup> Moreover, we can identify the  $V_{OC}$  and FF potential prior to and after proton irradiation to be at 1.85 V and 86%, respectively. With a  $J_{SC}$  of  $\approx 20.4 \text{ mA cm}^{-2}$  (as measured under AM0), we thus estimate an efficiency potential of 24% under AM0 illumination conditions for the here tested high-and low-gap perovskite combination and note that better light management, via textured foils or by anti-reflection coatings,<sup>[63]</sup> is a facile route to increase the efficiency potential towards the practical limit of 28.7%, cf. Figure 1b. Figure 4e,f shows measured  $JV$  curves in comparison to pseudo- $JV$  curves from Suns– $V_{OC}$  and Suns–QFLS measurements. Most importantly, the comparison of pseudo- $JV$  curves from Suns– $V_{OC}$  and Suns–QFLS of as-prepared to proton irradiated devices indicates negligible radiation-induced damage. To quantify

**Table 1.** Remaining efficiency ( $Q\eta$ ) of perovskite 2J tandem PV after proton irradiation: Remaining efficiency ( $Q\eta$ ) after accumulated proton doses of  $2 \times 10^{12}$  and  $1 \times 10^{13} \text{ p}^+ \text{ cm}^{-2}$ . Values were derived from MPP tracking and Suns– $V_{OC}$  measurements of the studied perovskite 2J tandem solar cells. Further, the summed Suns–QFLS data of bare high-gap and low-gap perovskite absorbers were used.

	Remaining efficiency ( $Q\eta$ ) after	
	$\Phi (\text{p}^+ \text{ cm}^{-2}) 2 \times 10^{12}$	$\Phi (\text{p}^+ \text{ cm}^{-2}) 1 \times 10^{13}$
$Q\eta$ (from MPP)	0.97	0.94
$Q\eta$ (from Suns– $V_{OC}$ pseudo- $JV$ )	1	1
$Q\eta$ (from Suns–QFLS pseudo- $JV$ )	1	1

this, we compare in Table 1 the remaining efficiency as derived from maximum power point tracking, Suns– $V_{OC}$ , and Suns–QFLS measurements. While MPP tracking suggests relative losses of around 6%, there are negligible radiation-induced losses apparent from pseudo- $JV$  curves extracted from Suns– $V_{OC}$  and Suns–QFLS data, which does not include contribution from contacts. This result once again suggests that the degradation of the contact layers limits the radiation hardness of the actual devices.

#### 4. Comparing Radiation-Induced Damage in III–V on Ge 3J and Perovskite 2J PV

To gain a more in-depth insight into the radiation-induced degradation, we compare the perovskite 2J tandem solar cell to III–V 3J on Ge triple-junction space PV. According to EQE measurements shown in Figure 2e, the GaAs middle cell degrades significantly under 68 MeV proton irradiation and, thereby, limiting the overall performance. To identify radiation-induced damage, we recorded PL images with high-spatial-resolution using a confocal PL microscope. We selectively collect the emission from the GaAs middle cell by employing a  $\lambda = 636 \text{ nm}$  excitation laser and appropriate optical filters for collection. On as-prepared reference samples, Figure 5a, we observe a highly uniform PL intensity as expected from an epitaxially grown layer on top of polished Ge wafers. However, after irradiation, we observe the formation of 500 nm-sized dark regions that appear and grow in number with increasing fluence. High energetic particle irradiation is known to damage along the ion track with a typical diameter between 1 and 20 nm, depending on the particle, energy, and material.<sup>[64]</sup> Etching along the track of weakened material can be used to produce membranes with precisely determined structure.<sup>[65]</sup> The size of the herein observed dark spots and the low density  $\approx 2 \times 10^7 \text{ cm}^{-2}$  compared to the accumulated proton dose of  $10^{13} \text{ p}^+ \text{ cm}^{-2}$ , however, suggests that the dark regions correspond to defect clusters rather than individual radiation-induced defects (see inset of Figure 5 and Figure S8, Supporting Information, for higher-resolution PL maps after proton irradiation). We note that the actual size of these clusters can be smaller than the observed dark regions as lateral diffusion of charge carriers to the trap sites can cause larger spots with reduced PL, and optical diffraction limits the resolution ( $\approx 300 \text{ nm}$  under the conditions here).

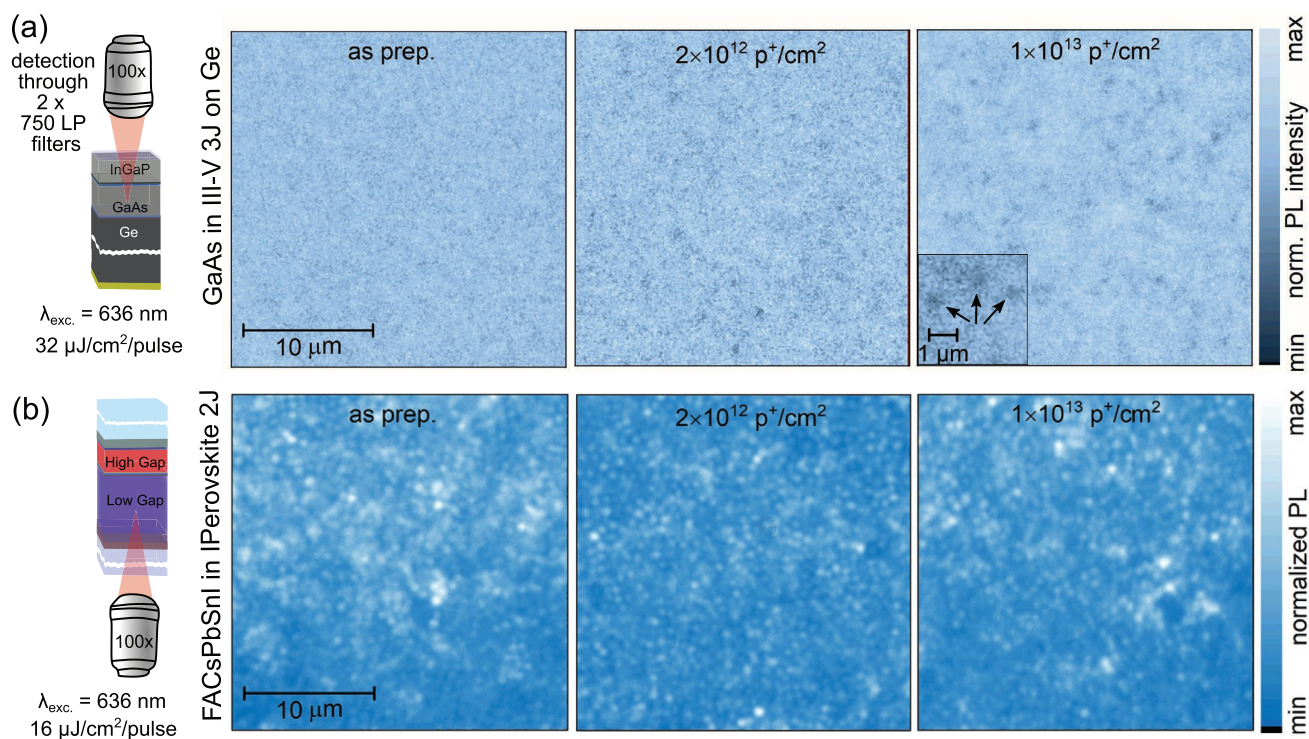


**Figure 5.** High-spatial resolution PL imaging of radiation-induced defect clusters in III–V 3J on Ge and perovskite 2J solar cells. a) Confocal photoluminescence map of the GaAs middle cell within the III–V 3J on Ge solar cell comprising InGaP/GaAs/Ge prior to and after proton irradiation. As indicated, excitation was performed through a 100× LWD objective using a 636 nm excitation that excited both the InGaP top and the GaAs middle cell. To selectively collect emission from the GaAs middle cell, two 750-nm LP filters were used. b) Confocal PL maps of the low-gap perovskite within the perovskite 2J solar cell. Here, excitation was performed from the backside slightly away from the Au electrode.

By contrast, similar high spatial resolution PL microscopy on the low-gap perovskite subcell, which dominates the degradation in the perovskite 2J cell (cf. EQE measurements in Figure 2d), do not reveal the formation of distinct dark spots after proton irradiation (Figure 5b and lifetime maps in Figure S8, Supporting Information), and the only luminescence variation is the underlying grain-to-grain variation owing to the polycrystalline nature of the perovskite films also seen in the reference samples.<sup>[66]</sup> This is consistent with the earlier findings from macroscopic PL measurements that any radiation-induced defects within the perovskite bulk do not play a significant role.

#### 4.1. Revealing the Dominant Degradation Mechanism in Perovskite 2J

We have shown that the perovskite 2J tandem technology studied within this paper, as well as the low- and wide-gap absorber layers themselves, exceed the resilience to high energetic radiation of the current industry-standard technology. The differences in hardness between the technologies emerge from the defect tolerance of the halide perovskite structure, in which the conduction band minimum (CBM) is formed by antibonding Pb p orbitals, while the valence band maximum (VBM) is comprising antibonding Pb s and I p orbitals.<sup>[67]</sup> The formation of defects in perovskites, e.g., by high-energy

irradiations, may create dangling bonds that are likely to appear as states within the bands while leaving the band gap free of new deep trap states.<sup>[68]</sup> Moreover, recent works have shown that defects in polycrystalline halide perovskite thin films are predominantly formed at interfaces between crystallographically and compositionally distinct entities in the form of nanoscale clusters,<sup>[69]</sup> which are unlikely to be altered by the irradiation conditions used herein. The VBM and CBM of traditional III–V semiconductors, in contrast, are formed by bonding and antibonding orbitals,<sup>[67]</sup> opening room for numerous deep traps that can be formed within the bandgap, making the material vulnerable to radiation damage. Needless to say, these properties are closely linked to the high material quality required in conventional (GaAs, Si) systems for high performance compared to polycrystalline halide perovskite, which exhibit a high degree of disorder yet work efficiently and are of high optoelectronic quality even when processed from solution. Moreover, low ion migration barriers<sup>[70]</sup> in halide perovskite allow efficient self-healing mechanisms even at room temperatures that have been observed under light<sup>[71]</sup> and high energetic irradiation.<sup>[13]</sup>

Nevertheless, we observe a small impact of radiation damage under AM0 conditions that can be traced to the low-gap perovskite subcell using EQE and absolute PL measurements that selectively probe the individual subcell within the tandem stack. Current mismatch under AM1.5G and Mars illumination conditions masks this degradation, thereby

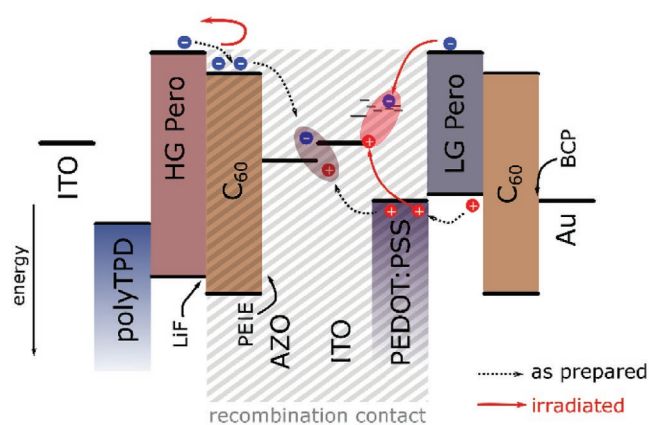


**Figure 6.** Simplified recombination contact of perovskite 2J tandem PV indicating the proposed working mechanism prior to irradiation and an example of unbalanced injection and additional recombination after high energy proton irradiation.

exemplifying that bandgap tuning of both the high and low-gap perovskite absorbers can be a powerful tool to tailor the radiation hardness of monolithic perovskite tandem solar cells for specific illumination conditions. In contrast to terrestrial applications, a high end-of-life performance is paramount for space applications, and lower beginning-of-life performances are happily accepted if this minimizes radiation-induced performance losses.

Measurements on bare low-gap perovskite absorbers further suggest negligible radiation-induced degradation as well as an unchanged efficiency and  $V_{OC}$  potential. High-resolution PL microscopy measurements exclude the formation of distinct defect clusters that are observed in GaAs within the irradiated III–V 3J on Ge solar cells. Therefore, the combined data strongly suggest that the degradation is linked to the recombination contact that interfaces both the high- and low-gap absorber layers; see highlighted area in **Figure 6**. Prior to irradiation, the recombination contact ensures that electrons from the high-gap perovskite and holes from the low-gap perovskite are efficiently annihilated. Formation of radiation-induced defects within the recombination contact as well as work function changes of the involved layers can lead to unbalanced injection and parasitic recombination with charge carriers from the same subcell. Such an unbalanced recombination contact would explain the paired PL enhancements and losses observed in the high- and low-gap subcells of the tandem layer stack, respectively.

The recombination contact comprises  $C_{60}$ /AZO/ITO/PEDOT:PSS, and, already for  $C_{60}$ , various groups have investigated the effect of radiation as it is part of the interstellar medium and can be found within comets and meteorites.<sup>[72]</sup> While  $C_{60}$  is described as relatively radiation hard, the polymerization to  $C_{120}$  dimers and  $C_{180}$  trimers, as well as a complete amorphization, are known under harsh/prolonged exposure.<sup>[73–75]</sup> In the case of ZnO and ITO, radiation-induced defects are known to decrease the conductivity, thereby affecting the performance of ITO transistors.<sup>[76,77]</sup> On the other hand, the electrical conductivity of PEDOT:PSS has been shown to increase upon UV,<sup>[78]</sup>  $\gamma$ -ray,<sup>[79]</sup> and high energy electron irradiation<sup>[80]</sup> due to radiation-induced crosslinking and oxidation (doping). Moreover, recent reports on thermal degradation

of PEDOT:PSS/low-gap perovskite systems have shown that PEDOT:PSS can cause the oxidation of Sn of the low-gap Pb–Sn alloyed perovskite, likely activated from the surface.<sup>[26,81]</sup> Therefore, in the specific architecture and as shown in **Figure 6**, the damaged recombination layer may lead to a barrier to charge quenching from the high-gap perovskite to the  $C_{60}$ , thus increasing the PL intensity of that absorber relative to the pristine control, while the damaged, more-conductive PEDOT will better quench the PL from the low-gap cell (cf. **Figure 4a**). The collective results highlight that the perovskite tandem absorber layers are sufficiently radiation-hard, but more robust, radiation-hard recombination contacts must be identified to unleash the full potential of all-perovskite tandem solar cells for space applications.

## 5. Challenges

While resilience to high energy radiation is the key requirement for adopting any emerging PV technology in space, there are many additional environmental extremes that space PV modules need to withstand. Most prominently, these are solar UV radiation, high vacuum, extreme temperatures and temperature cycles, as well as atomic oxygen (AtOx) in low-Earth orbit, and low-intensity low-temperature (LILT) environments in the vicinity of Jupiter, Saturn, and deep space.<sup>[82–84]</sup> In the following, we will discuss the importance of these additional environmental stresses for perovskite-based tandem PV technologies. Perovskite solar cells are commonly made in superstrate configuration in which illumination is performed through the substrate, and the backside is encapsulated to protect them from moisture and oxygen.<sup>[85]</sup> We measured the transmission of commonly used rigid and flexible substrate materials, see **Figure S10** (Supporting Information), and found that those substrates effectively block harsh vacuum-UV, UV-C, and UV-B radiation. Such short wave UV light is otherwise capable of damaging the often used organic contact layers<sup>[86]</sup> and the perovskite itself, particularly in the case of methylammonium-based compositions.<sup>[87]</sup> To also block UV-A light, we propose the use of down-converters on or within the substrate that have successfully prolonged the stability of particular UV-A sensitive perovskite compositions/architectures and further improved their power conversion efficiencies.<sup>[88–91]</sup> The same substrate and encapsulation solutions can further be practical barriers to AtOx formed by photodissociated  $O_2$  in the upper earth atmosphere. However, the substrate and encapsulation materials themselves must be made from polymers that withstand harsh UV and AtOx to avoid scissioning and chemical erosion of the substrate and encapsulation.<sup>[84]</sup> Promising candidates are fluorinated polymers or the use of protection layers.<sup>[84,91]</sup> The substrate/encapsulation material choice will also define the outgassing of volatile components, additives, adsorbed gases, or degradation products.<sup>[84]</sup> An entirely different challenge are extreme temperature cycles between  $-100$  and  $+90$  °C during eclipse and full AM0 illumination that cannot be avoided. Especially methylammonium lead iodide perovskites undergo phase transitions in this temperature regime, and many works have speculated that this might become problematic during temperature cycles.<sup>[92,93]</sup>

Quite contrary to that, recent works showed that cycling to low temperatures activates a self-elimination of intrinsic defects in compositionally engineered perovskite compositions, such as the high- and low-gap compositions used herein, boosting the  $V_{OC}$  and  $\eta$  after temperature cycling beyond as prepared values.<sup>[94]</sup> While these measurements have been performed down to 180 K under AM0 illumination in an aerospace simulation chamber,<sup>[94]</sup> other works have recently simulated the low-temperature ( $\approx 100$  and 135 K) and low-intensity (0.011 and 0.037 AM0) (LILT) environments found at Saturn and Jupiter orbits.<sup>[83]</sup> Their results demonstrated the promise of perovskite-based PV systems for LILT environments and deep space missions.<sup>[83]</sup> Unlike many traditional PV technologies that possess low temperature coefficients of around  $-0.3\% \text{ K}^{-1}$  (CIGS, Si, III–V 3J),<sup>[95]</sup> halide-based perovskites have smaller values around  $-0.1\% \text{ K}^{-1}$  making them attractive candidates for low-temperature environments.<sup>[83,94]</sup> The other extreme is high temperatures. While this challenge is well mimicked in standard accelerated aging tests of perovskite PV for terrestrial use cases, summarized elsewhere,<sup>[96–101]</sup> we note the absence of convection cooling, which requires optimization of the IR emissivity. In flexible CIGS space PV, this has been solved using polysiloxane coatings.<sup>[102]</sup>

## 6. Conclusion

In conclusion, we have identified all-perovskite multijunction PV to have immense potential for next-generation ultralight-weight, flexible, but cost-efficient space photovoltaics. Processed on flexible foils, their specific power outperforms today's space PV, III–V 3J on Ge technologies. We demonstrate via in situ measurements during high energetic proton irradiation that the ability of all-perovskite tandems to withstand the harsh radiation environment in space exceeds those of commercially available III–V 3J on Ge systems. The perovskite 2J tandem solar cells retain over 94% of their initial efficiency under AM0 after high energy proton irradiation at an accumulated dose of  $1 \times 10^{13} \text{ p}^+ \text{ cm}^{-2}$  equivalent to the accumulated dose after >100 years in near-earth and >10 years in geostationary orbit. Tested III–V 3J solar cells on Ge, the yet unparalleled industry-standard technology combining high radiation hardness and high efficiency, in contrast, degrade by more than 22% under identical conditions. By measuring the EQE of the individual subcells, we identify the low-gap perovskite bottom cell (albeit small overall damage) and the GaAs middle cell (large overall damage) are most susceptible to radiation-induced damage within those two systems. We reveal radiation-induced defect clusters in high-resolution PL microscopy within the GaAs middle cell, which we do not observe upon proton irradiation in the low-gap perovskite bottom cell. In contrast, we show that the  $V_{OC}$ , FF, and efficiency potential of high- and low-gap perovskite compositions required for efficient perovskite 2J tandem PV remain high and unchanged. We propose, based on our combined electrical and optical characterizations, that the recombination contact formed by a sandwich of organic and inorganic materials becomes slightly damaged. At the same time, the individual high- and low-gap perovskite absorbers themselves remain unaffected. Radiation-induced damage in

the compared III–V and perovskite-based technologies, therefore, follow distinct mechanisms.

## 7. Experimental Section

Full details of experimental procedures can be found in the Supporting Information.

## Supporting Information

Supporting Information is available from the Wiley Online Library or from the author.

## Acknowledgements

F.L. acknowledges financial support from the Alexander von Humboldt Foundation via the Feodor Lynen program and is grateful to Prof. Sir R. Friend for supporting his Fellowship at the Cavendish Laboratory. G.E.E. was funded by NREL's LDRD program. This work was further supported by the European Research Council (ERC) under the European Union's Horizon 2020 research and innovation program (HYPERION, Grant Agreement No. 756962). A.A.-A. acknowledges financial support from the German Federal Ministry of Education and Research (BMBF) via program "Materialforschung für die Energiewende" (Grant No. 03SF0540), by the German Federal Ministry for Economic Affairs and Energy (BMWi) through the "PersiST" project (Grant No. 0324037C). K.F. acknowledges the George and Lilian Schiff Fund, the Engineering and Physical Sciences Research Council (EPSRC), the Winton Sustainability Fellowship, and the Cambridge Trust for funding. S.D.S. acknowledges the Royal Society and Tata Group (UF150033). The authors acknowledge the EPSRC for funding (EP/R023980/1). This project received funding from the European Union's Horizon 2020 research and innovation program under the Marie Skłodowska-Curie Grant Agreement No. 841265. The authors acknowledge Axel Palmstrom and William Nemeth at NREL for depositing some of the layers in the tandem stack.

## Conflict of Interest

S.D.S. and G.E.E. are co-founders of Swift Solar, Inc., a company commercializing high-power, lightweight perovskite solar panels.

## Author Contributions

F.L. initiated the research and planned the experiments with input from G.E.E. H.-C.N., and S.D.S. G.K., J.B., and A.D. performed the proton irradiation experiments. F.L. recorded the in situ data. G.E.E. fabricated all-perovskite tandem devices and perovskite thin films. F.L. performed the photovoltaic characterizations with help from A.A.A. F.L. and E.M.T. performed the hyperspectral PL measurements. K.F. helped with QFLS calculations. F.L. recorded PL lifetime maps of the perovskite and GaAs subcells. F.L. simulated the energy loss using SRIM. F.L. analyzed all data and took the lead in drafting the manuscript. F.L., G.E., and S.D.S. wrote the paper with input from other authors. All authors contributed to the discussion of the results.

## Data Availability Statement

The data that support the findings of this study are available from the corresponding authors upon reasonable request.

## Keywords

all-perovskite tandem photovoltaics, proton-irradiation, radiation hardness, solar cells, space photovoltaics

Received: July 23, 2021

Revised: September 3, 2021

Published online: September 21, 2021

- [1] R. L. Easton, M. J. Votaw, *Rev. Sci. Instrum.* **1959**, *30*, 70.
- [2] Azur Space Solar Power GmbH, <http://www.azurspace.com/index.php/en/> (accessed: September 2019).
- [3] W. Guter, F. Dunzer, L. Ebel, K. Hillerich, W. Köstler, T. Kubera, M. Meusel, B. Postels, C. Wächter, *E3S Web Conf.* **2017**, *16*, 03005.
- [4] Spectrolab, <https://www.spectrolab.com/index.html> (accessed: September 2019).
- [5] MicroLink Devices, <http://mldevices.com> (accessed: September 2020).
- [6] N. Miyashita, N. Ahsan, Y. Okada, R. Tatavarti, A. Wibowo, N. Pan, *Conf. Rec. IEEE Photovolt. Spec. Conf.* **2019**, 1502.
- [7] H. C. Neitzert, L. Labonia, M. Citro, P. Delli Veneri, L. Mercaldo, *Phys. Status Solidi* **2010**, *7*, 1065.
- [8] K. Zajac, S. Brunner, C. A. Kaufmann, R. Caballero, A. Rahm, C. Scheit, H. Zachmann, F. Kessler, M. Wagner, *2009 34th IEEE Photovolt. Spec. Conf.* **2009**, 000055.
- [9] D. L. Bätzner, A. Romeo, M. Terheggen, M. Döbeli, H. Zogg, A. N. Tiwari, *Thin Solid Films* **2004**, *451*, 536.
- [10] L. K. Reb, M. Böhmer, B. Predeschly, S. Grott, C. L. Weindl, G. I. Ivandekic, R. Guo, C. Dreißigacker, R. Gernhäuser, A. Meyer, P. Müller-Buschbaum, *Joule* **2020**, *92*, 074501.
- [11] I. Cardinaletti, T. Vangerven, S. Nagels, R. Cornelissen, D. Schreurs, J. Hruba, J. Vodnik, D. Devisscher, J. Kesters, J. D'Haen, A. Franquet, V. Spampinato, T. Conard, W. Maes, W. Deferme, J. V. Manca, *Sol. Energy Mater. Sol. Cells* **2018**, *182*, 121.
- [12] J. Barbé, D. Hughes, Z. Wei, A. Pockett, H. K. H. Lee, K. C. Heasman, M. J. Carnie, T. M. Watson, W. C. Tsoi, *Sol. RRL* **2019**, *3*, 1900219.
- [13] F. Lang, N. H. Nickel, J. Bundesmann, S. Seidel, A. Denker, S. Albrecht, V. V. Brus, J. Rappich, B. Rech, G. Landi, H. C. Neitzert, *Adv. Mater.* **2016**, *28*, 8726.
- [14] F. Lang, M. Jošt, J. Bundesmann, A. Denker, S. Albrecht, G. Landi, H. C. Neitzert, J. Rappich, N. H. Nickel, *Energy Environ. Sci.* **2019**, *12*, 1634.
- [15] S. Kanaya, G. M. Kim, M. Ikegami, T. Miyasaka, K. Suzuki, Y. Miyazawa, H. Toyota, K. Osonoe, T. Yamamoto, K. Hirose, *J. Phys. Chem. Lett.* **2019**, *10*, 6990.
- [16] Y. Miyazawa, M. Ikegami, H.-W. Chen, T. Ohshima, M. Imaizumi, K. Hirose, T. Miyasaka, *iScience* **2018**, *2*, 148.
- [17] O. Malinkiewicz, M. Imaizumi, S. B. Sapkota, T. Ohshima, S. Öz, *Emergent Mater.* **2020**, *3*, 9.
- [18] F. Lang, M. Jošt, M. Frohna, E. Köhnen, A. Al-Ashouri, A. R. Bowman, T. Bertram, A. B. Morales-Vilches, D. Koushik, E. M. Tennyson, K. Galkowski, G. Landi, M. Creatore, B. Stannowski, C. A. Kaufmann, J. Bundesmann, J. Rappich, B. Rech, A. Denker, S. Albrecht, H.-C. Neitzert, N. H. Nickel, S. D. Stranks, *Joule* **2020**, *4*, 1054.
- [19] M. T. Hörantner, T. Leijtens, M. E. Ziffer, G. E. Eperon, M. G. Christoforo, M. D. McGehee, H. J. Snaith, *ACS Energy Lett.* **2017**, *2*, 2506.
- [20] T. Moot, J. Werner, G. E. Eperon, K. Zhu, J. J. Berry, M. D. McGehee, J. M. Luther, *Adv. Mater.* **2020**, *32*, 2003312.
- [21] A. F. Palmstrom, G. E. Eperon, T. Leijtens, R. Prasanna, S. N. Habisreutinger, W. Nemeth, E. A. Gaulding, S. P. Dunfield, M. Reese, S. Nanayakkara, T. Moot, J. Werner, J. Liu, B. To, S. T. Christensen, M. D. McGehee, M. F. A. M. van Hest, J. M. Luther, J. J. Berry, D. T. Moore, *Joule* **2019**, *3*, 2193.
- [22] E. T. Hoke, D. J. Slotcavage, E. R. Dohner, A. R. Bowring, H. I. Karunadasa, M. D. McGehee, *Chem. Sci.* **2015**, *6*, 613.
- [23] G. E. Eperon, K. H. Stone, L. E. Mundt, T. H. Schloemer, S. N. Habisreutinger, S. P. Dunfield, L. T. Schelhas, J. J. Berry, D. T. Moore, *ACS Energy Lett.* **2020**, 1856.
- [24] Y. Miyazawa, M. Ikegami, T. Miyasaka, T. Ohshima, M. Imaizumi, K. Hirose, in *2015 IEEE 42nd Photovoltaic Specialist Conference (PVSC)*, IEEE, **2015**, pp. 1–4.
- [25] C. G. Bischak, C. L. Hetherington, H. Wu, S. Aloni, D. F. Ogletree, D. T. Limmer, N. S. Ginsberg, *Nano Lett.* **2017**, *17*, 1028.
- [26] L. E. Mundt, J. Tong, A. F. Palmstrom, S. P. Dunfield, K. Zhu, J. J. Berry, L. T. Schelhas, E. L. Ratcliff, *ACS Energy Lett.* **2020**, *5*, 3344.
- [27] A. G. Boldyreva, A. F. Akbulatov, S. A. Tsarev, S. Y. Luchkin, I. S. Zhidkov, E. Z. Kurmaev, K. J. Stevenson, V. G. Petrov, P. A. Troshin, A. G. Boldyreva, S. Y. Luchkin, V. G. Petrov, S. A. Tsarev, A. F. Akbulatov, P. A. Troshin, E. Z. Kurmaev, I. S. Zhidkov, S. A. Tsarev, S. Y. Luchkin, I. S. Zhidkov, E. Z. Kurmaev, K. J. Stevenson, V. G. Petrov, P. A. Troshin, *J. Phys. Chem. Lett.* **2019**, *10*, 813.
- [28] G. Schiwietz, K. Czerski, M. Roth, F. Staufenbiel, P. L. Grande, *Nucl. Instrum. Methods Phys. Res., Sect. B* **2004**, *226*, 683.
- [29] NREL, "Research Cell Efficiency Records," **2021**.
- [30] M. Jošt, L. Kegelmann, L. Korte, S. Albrecht, *Adv. Energy Mater.* **2020**, *10*, 1904102.
- [31] A. Chirilă, S. Buecheler, F. Pianezzi, P. Bloesch, C. Gretener, A. R. Uhl, C. Fella, L. Kranz, J. Perrenoud, S. Seyrling, R. Verma, S. Nishiwaki, Y. E. Romanyuk, G. Bilger, A. N. Tiwari, *Nat. Mater.* **2011**, *10*, 857.
- [32] M. A. Green, E. D. Dunlop, J. Hohl-Ebinger, M. Yoshita, N. Kopidakis, X. Hao, *Prog. Photovoltaics Res. Appl.* **2021**, 657.
- [33] A. Banerjee, X. Xu, K. Beernink, F. Liu, K. Lord, G. Demaggio, B. Yan, T. Su, G. Pietka, C. Worrel, S. Ehlert, D. Beglau, J. Yang, S. Guha, *Conf. Rec. IEEE Photovolt. Spec. Conf.* **2010**, 2651.
- [34] P. R. Sharps, A. Cornfeld, M. Stan, A. Korostyshevsky, V. Ley, B. Cho, T. Varghese, J. Diaz, D. Aiken, *Conf. Rec. IEEE Photovolt. Spec. Conf.* **2008**, <https://doi.org/10.1109/PVSC.2008.4922854>
- [35] D. J. Aiken, A. B. Cornfeld, M. A. Stan, P. R. Sharps, *Conf. Rec. 2006 IEEE 4th World Conf. Photovolt. Energy Conversion WCPEC-4* **2006**, *1*, 838.
- [36] M. Kaltenbrunner, G. Adam, E. D. Głowacki, M. Drack, R. Schwödauer, L. Leonat, D. H. Apaydin, H. Groiss, M. C. Scharber, M. S. White, N. S. Sariciftci, S. Bauer, *Nat. Mater.* **2015**, *14*, 1032.
- [37] J. Ramanujam, D. M. Bishop, T. K. Todorov, O. Gunawan, J. Rath, R. Nekovei, E. Artegiani, A. Romeo, *Prog. Mater. Sci.* **2020**, *110*, 100619.
- [38] S. Brunner, K. Zajac, M. Nadler, K. Seifart, C. A. Kaufmann, H. Schock, L. Hartmann, K. Otte, A. Rahm, C. Scheit, *9th European Space Power Conference*, October **2011**, <https://ui.adsabs.harvard.edu/abs/2011ESASP.690E.135B>.
- [39] K. Otte, L. Makhova, A. Braun, I. Kononov, *Thin Solid Films* **2006**, *511*, 613.
- [40] F. Fu, S. Nishiwaki, J. Werner, T. Feurer, S. Pisoni, Q. Jeangros, S. Buecheler, C. Ballif, A. N. Tiwari, *arXiv:1907.10330*, **2019**.
- [41] L. A. Zafoschnig, S. Nold, J. C. Goldschmidt, *IEEE J. Photovoltaics* **2020**, 1632.
- [42] A. Akkerman, J. Barak, M. B. Chadwick, J. Levinson, M. Murat, Y. Lifshitz, *Radiat. Phys. Chem.* **2001**, *62*, 301.
- [43] C. Baur, M. Gervasi, P. Nieminen, P. G. Rancoita, M. Tacconi, *Eur. Space Power Conf. 2014* **2014**, *2014*, 15.

- [44] J. P. Babaro, K. G. West, B. H. Hamadani, *Energy Sci. Eng.* **2016**, 4, 372.
- [45] G. Siefer, C. Baur, A. W. Bett, *Conf. Rec. IEEE Photovolt. Spec. Conf.* **2010**, 704.
- [46] C. Inguibert, S. Messenger, *IEEE Trans. Nucl. Sci.* **2012**, 59, 3117.
- [47] J. Xu, M. Guo, M. Lu, H. He, G. Yang, J. Xu, *Materials* **2018**, 11, 944.
- [48] R. Campesato, C. Baur, M. Carta, M. Casale, D. Chiesa, M. Gervasi, E. Gombia, E. Greco, A. Kingma, M. Nastasi, E. Previtali, P. G. Rancoita, D. Rozza, E. Santoro, M. Tacconi, *Conf. Rec. IEEE Photovolt. Spec. Conf.* **2019**, 2381.
- [49] W. C. Dash, R. Newman, *Phys. Rev.* **1955**, 99, 1151.
- [50] J. F. Ziegler, M. D. D. Ziegler, J. P. P. Biersack, *Nucl. Instrum. Methods Phys. Res., Sect. B* **2010**, 268, 1818.
- [51] S. R. Messenger, E. A. Burke, R. J. Walters, J. H. Warner, G. P. Summers, *Prog. Photovoltaics Res. Appl.* **2005**, 13, 115.
- [52] SPENVIS, Space Environment Information System, funded by the European Space Agency (ESA), <http://www.spennis.ome.be/spennis> (accessed: September 2019).
- [53] C. Paranicas, J. F. Cooper, H. B. Garrett, R. E. Johnson, S. J. Sturmer, *Europa* **2017**, 529.
- [54] D. Matthiä, B. Ehresmann, H. Lohf, J. Köhler, C. Zeitlin, J. Appel, T. Sato, T. Slaba, C. Martin, T. Berger, E. Boehm, S. Boettcher, D. E. Brinza, S. Burmeister, J. Guo, D. M. Hassler, A. Posner, S. C. R. Rafkin, G. Reitz, J. W. Wilson, R. F. Wimmer-Schweingruber, *J. Space Weather Space Clim.* **2016**, 6, A13.
- [55] G. A. Landis, D. Hyatt, *Conf. Rec. 2006 IEEE 4th World Conf. Photovolt. Energy Conversion WCPEC-4* **2006**, 2, 1979.
- [56] P. Würfel, *J. Phys. C: Solid State Phys.* **1982**, 15, 3967.
- [57] M. Stolterfoht, C. M. Wolff, J. A. Márquez, S. Zhang, C. J. Hages, D. Rothhardt, S. Albrecht, P. L. Burn, P. Meredith, T. Unold, D. Neher, *Nat. Energy* **2018**, 3, 847.
- [58] D. Guo, V. M. Caselli, E. M. Hutter, T. J. Savenije, *ACS Energy Lett.* **2019**, 4, 855.
- [59] J. K. Katahara, H. W. Hillhouse, *J. Appl. Phys.* **2014**, 116, 173504.
- [60] M. Stolterfoht, M. Grischek, P. Caprioglio, C. M. Wolff, E. Gutierrez-Partida, F. Peña-Camargo, D. Rothhardt, S. Zhang, M. Raoufi, J. Wolansky, M. Abdi-Jalebi, S. D. Stranks, S. Albrecht, T. Kirchartz, D. Neher, *Adv. Mater.* **2020**, 32, 2000080.
- [61] S. R. Cowan, A. Roy, A. J. Heeger, *Phys. Rev. B* **2010**, 82, 245207.
- [62] V. V. Brus, F. Lang, J. Bundesmann, S. Seidel, A. Denker, B. Rech, G. Landi, H. C. Neitzert, J. Rappich, N. H. Nickel, *Adv. Electron. Mater.* **2017**, 3, 1600438.
- [63] M. Jošt, S. Albrecht, L. Kegelman, C. M. Wolff, F. Lang, B. Lipovšek, J. Krč, L. Korte, D. Neher, B. Rech, M. Topič, *ACS Photonics* **2017**, 4, 1232.
- [64] J. Ackermann, N. Angert, R. Neumann, C. Trautmann, M. Dischner, T. Hagen, M. Sedlacek, *Nucl. Instrum. Methods Phys. Res., Sect. B* **1996**, 107, 181.
- [65] P. Apel, *Radiat. Meas.* **2001**, 34, 559.
- [66] E. M. Tennyson, T. A. S. Doherty, S. D. Stranks, *Nat. Rev. Mater.* **2019**, 4, 573.
- [67] H. Jin, E. Debroye, M. Keshavarz, I. G. Scheblykin, M. B. J. J. Roeffaers, J. Hofkens, J. A. Steele, J. Hofkens, J. A. Steele, *Mater. Horiz.* **2019**, 7, 397.
- [68] R. E. Brandt, V. Stevanović, D. S. Ginley, T. Buonassisi, *MRS Commun.* **2015**, 5, 265.
- [69] T. A. S. Doherty, A. J. Winchester, S. Macpherson, D. N. Johnstone, V. Pareek, E. M. Tennyson, S. Kosar, F. U. Kosasih, M. Anaya, M. Abdi-Jalebi, Z. Andaji-Garmaroudi, E. L. Wong, J. Madéo, Y. H. Chiang, J. S. Park, Y. K. Jung, C. E. Petoukhoff, G. Divitini, M. K. L. Man, C. Ducati, A. Walsh, P. A. Midgley, K. M. Dani, S. D. Stranks, *Nature* **2020**, 580, 360.
- [70] Y. Yuan, J. Huang, *Acc. Chem. Res.* **2016**, 49, 286.
- [71] D. R. Ceratti, A. V. Cohen, R. Tenne, Y. Rakita, L. Snarski, L. Cremonesi, I. Goldian, I. Kaplan-Ashiri, T. Bendikov, V. Kalchenko, M. Elbaum, M. A. C. Potenza, L. Kronik, G. Hodes, D. Cahen, *Mater. Horiz.* **2021**, 8, 1570.
- [72] F. Cataldo, G. Strazzulla, S. Iglesias-Groth, *Mon. Not. R. Astron. Soc.* **2009**, 394, 615.
- [73] J. Onoe, T. Nakayama, M. Aono, T. Hara, *Appl. Phys. Lett.* **2003**, 82, 595.
- [74] R. G. Musket, R. A. Hawley-Fedder, W. L. Bell, *Radiat. Eff. Defects Solids* **1991**, 118, 225.
- [75] A. Yogo, T. Majima, A. Itoh, *Nucl. Instrum. Methods Phys. Res., Sect. B* **2002**, 193, 299.
- [76] Y. K. Moon, S. Lee, D. Y. Moon, W. S. Kim, B. W. Kang, J. W. Park, *Surf. Coat. Technol.* **2010**, 205, S109.
- [77] K. Koike, T. Aoki, R. Fujimoto, S. Sasa, M. Yano, S. ichi Gonda, R. Ishigami, K. Kume, *Phys. Status Solidi* **2012**, 9, 1577.
- [78] H. K. Lee, J. K. Kim, O. O. Park, *Org. Electron.* **2009**, 10, 1641.
- [79] H. Jang, J. Park, F. S. Kim, *Phys. Status Solidi* **2019**, 216, 1800980.
- [80] N. Chaudhary, A. Singh, D. K. Aswal, M. Bharti, A. Sharma, A. R. Tillu, M. Roy, B. P. Singh, J. Bahadur, V. Putta, A. K. Debnath, *Polymer* **2020**, 202, 122645.
- [81] R. Prasanna, T. Leijtens, S. P. Dunfield, J. A. Raiford, E. J. Wolf, S. A. Swifter, J. Werner, G. E. Eperon, C. de Paula, A. F. Palmstrom, C. C. Boyd, M. F. A. M. van Hest, S. F. Bent, G. Teeter, J. J. Berry, M. D. McGehee, *Nat. Energy* **2019**, 4, 939.
- [82] J. Yang, Q. Bao, L. Shen, L. Ding, *Nano Energy* **2020**, 76, 105019.
- [83] C. R. Brown, G. E. Eperon, V. R. Whiteside, I. R. Sellers, *ACS Appl. Energy Mater.* **2018**, 2, 814.
- [84] E. Grossman, I. Gouzman, *Nucl. Instrum. Methods Phys. Res., Sect. B* **2003**, 208, 48.
- [85] R. Cheacharoen, C. C. Boyd, G. F. Burkhard, T. Leijtens, J. A. Raiford, K. A. Bush, S. F. Bent, M. D. McGehee, *Sustainable Energy Fuels* **2018**, 2, 2398.
- [86] A. Classen, T. Heumueller, I. Wabra, J. Gerner, Y. He, L. Einsiedler, N. Li, G. J. Matt, A. Osvet, X. Du, A. Hirsch, C. J. Brabec, *Adv. Energy Mater.* **2019**, 9, 1902124.
- [87] N. H. Nickel, F. Lang, V. V. Brus, O. Shargaieva, J. Rappich, *Adv. Electron. Mater.* **2017**, 3, 1700158.
- [88] N. U. Rahman, W. Khan, S. Khan, X. Chen, J. Khan, J. Zhao, Z. Yang, M. Wu, Z. Chi, *J. Mater. Chem. A* **2019**, 7, 6467.
- [89] H. S. Roh, G. S. Han, S. Lee, S. Kim, S. Choi, C. Yoon, J. K. Lee, *J. Power Sources* **2018**, 389, 135.
- [90] T. Leijtens, G. E. Eperon, S. Pathak, A. Abate, M. M. Lee, H. J. Snaith, *Nat. Commun.* **2013**, 4, 2885.
- [91] F. Bella, G. Griffini, J.-P. Correa-Baena, G. Saracco, M. Grätzel, A. Hagfeldt, S. Turri, C. Gerbaldi, *Science* **2016**, 354, 203.
- [92] X. Kong, K. Shayan, S. Lee, C. Ribeiro, S. Strauf, S. S. Lee, *Nanoscale* **2018**, 10, 8320.
- [93] C. Qin, T. Matsushima, D. Klotz, T. Fujihara, C. Adachi, *Adv. Sci.* **2019**, 6, 1801079.
- [94] Y. Chen, S. Tan, N. Li, B. Huang, X. Niu, L. Li, M. Sun, Y. Zhang, X. Zhang, C. Zhu, N. Yang, H. Zai, Y. Wu, S. Ma, Y. Bai, Q. Chen, F. Xiao, K. Sun, H. Zhou, *Joule* **2020**, 4, 1961.
- [95] E. F. Fernández, G. Siefer, M. Schachtner, A. J. García Loureiro, P. Pérez-Higueras, *AIP Conf. Proc.* **2012**, 1477, 189.
- [96] M. V. Khenkin, E. A. Katz, A. Abate, G. Bardizza, J. J. Berry, C. Brabec, F. Brunetti, V. Bulović, Q. Burlingame, A. Di Carlo, R. Cheacharoen, Y. B. Cheng, A. Colmann, S. Cros, K. Domanski, M. Dusza, C. J. Fell, S. R. Forrest, Y. Galagan, D. Di Girolamo, M. Grätzel, A. Hagfeldt, E. von Hauff, H. Hoppe, J. Kettle, H. Köbler, M. S. Leite, S. (Frank) Liu, Y. L. Loo, J. M. Luther, C. Q. Ma, M. Madsen, M. Manceau, M. Matheron, M. McGehee, R. Meitzner, M. K. Nazeeruddin, A. F. Nogueira, Ç. Odabaşı, A. Osherov, N. G. Park, M. O. Reese, F. De Rossi, M. Saliba,

- U. S. Schubert, H. J. Snaith, S. D. Stranks, W. Tress, P. A. Troshin, V. Turkovic, S. Veenstra, I. Visoly-Fisher, A. Walsh, T. Watson, H. Xie, R. Yildirim, S. M. Zakeeruddin, K. Zhu, M. Lira-Cantu, *Nat. Energy* **2020**, *5*, 35.
- [97] X. Zheng, A. Y. Alsalloum, Y. Hou, E. H. Sargent, O. M. Bakr, *Acc. Mater. Res.* **2020**, *1*, 63.
- [98] Z. Zhao, F. Gu, H. Rao, S. Ye, Z. Liu, Z. Bian, C. Huang, *Adv. Energy Mater.* **2018**, *9*, 1802671.
- [99] S. P. Dunfield, L. Bliss, F. Zhang, J. M. Luther, K. Zhu, M. F. A. M. van Hest, M. O. Reese, J. J. Berry, *Adv. Energy Mater.* **2020**, *10*, 1904054.
- [100] M. Z. Rahman, T. Edvinsson, *Matter* **2019**, *1*, 550.
- [101] F. Lang, O. Shargaieva, V. V. Brus, H. C. Neitzert, J. Rappich, N. H. Nickel, *Adv. Mater.* **2018**, *30*, 1702905.
- [102] M. Günthner, M. Pscherer, C. Kaufmann, G. Motz, *Sol. Energy Mater. Sol. Cells* **2014**, *123*, 97.